Article

Numerically Calculated 3-D Space-Weighting Functions to Image Crustal Volcanic Structures Using Diffuse Coda Waves

Edoardo Del Pezzo [1,†], Angel De La Torre [2], Francesca Bianco [3], Jesús Ibanez [4], Simona Gabrielli [5] and Luca De Siena [6*]

[1] Instituto Andaluz de Geofisica, University of Granada. Campus de Cartuja. Granada, Spain; edoardo.delpezzo@ingv.it
[2] Departamento de Teoria de la Senal Telematica y Comunicaciones, C/ Periodista Daniel Saucedo Aranda, s/n, Universidad de Granada, Spain; atv@ugr.es
[3] Istituto Nazionale di Geofisica e Vulcanologia sezione di Napoli, Napoli, Italy; francesca.bianco@ingv.it
[4] Instituto Andaluz de Geofisica, University of Granada. Campus de Cartuja. Granada, Spain; jibanez@ugr.es
[5] Dept. of Geology and Petroleum Geology, School of Geosciences, University of Aberdeen, Aberdeen, United Kingdom; simona.gabrielli@abdn.ac.uk
[6] Dept. of Geology and Petroleum Geology, School of Geosciences, University of Aberdeen, Aberdeen, United Kingdom; lucadesiena@abdn.ac.uk
* Correspondence: lucadesiena@abdn.ac.uk; Tel.: +44 (0)1224 273455
† Also at: Istituto Nazionale di Geofisica e Vulcanologia sezione di Napoli, Napoli, Italy

Academic Editor: Janire Prudencio
Version April 30, 2018 submitted to Geosciences

Abstract: Seismic coda measurements retrieve parameters linked to the physical characteristics of the rock volumes illuminated by high-frequency scattered waves. Space Weighting Functions (SWF) and kernels are different tools, which model the spatial sensitivity of coda envelopes to scattering and absorption anomalies in these rock matrices, allowing coda-wave attenuation (Q_{coda}) imaging. This note clarifies the difference between SWF and sensitivity kernels developed for coda wave imaging. It extends to the third dimension the SWF previously developed in 2D using radiative transfer and diffusion equation, based on the assumption of Q_{coda} variations dependent solely on variations of the extinction length. When applied to active data (Deception Island, Antarctica), 3D SWF images strongly resemble 2D images, making this 3D extension redundant. On the other hand, diffusion does not efficiently model coda waveforms when using earthquake datasets spanning depths between 0 and 20 km, as at Mount St. Helens volcano. In this setting, scattering attenuation and absorption suffer trade-off and cannot be separated by fitting a single seismogram energy envelope for SWF imaging. We propose that an approximate analytical 3D SWF, similar in shape to common coda kernels used in literature, can still be used in a space-weighted back-projection approach. While Q_{coda} is not a physical parameter of the propagation medium, its spatially-dependent modelling allows improved reconstruction of crustal-scale tectonic and geological features. It is even more efficient as a velocity-independent imaging tool for magma and fluid storage, once applied to deep volcanism.

Keywords: Seismic Attenuation; Seismic Coda; Seismic Scattering; Diffusion; Coda Imaging

1. Introduction

[1]

Seismic attenuation imaging performed using coda waves provides novel information about tectonic structures and fluid content at crustal [1,2], regional [3] and local [4] scales. The attenuation coefficient is proportional to the sum of the inverse intrinsic (Q_i^{-1}) and scattering (Q_s^{-1}) quality factors. A separate estimate of scattering attenuation and absorption is crucial for understanding seismic wave propagation in highly-heterogeneous volcanic environments [eg 5] or when targeting areas having different tectonic and scattering properties at crustal and lithospheric scales [eg 6–8]. A scattering ellipsoid has been adopted for decades by scientists to map the sensitivity of coda waves to Earth heterogeneities, and map scattering attenuation and absorption in space [eg 9]. More recently, 2D and 3D coda sensitivity kernels based on multiple scattering propagation have been proposed to separate Q_i^{-1} and Q_s^{-1} [eg 8,10] and invert for attenuation in the subsurface at different scales and considering depth [eg 2,11,12]. These sensitivity kernels define the source parameters observed at a station as a space-weighted average of attenuation characteristics of the sampled medium, where the weights are defined via integral equations [10,12]. Their application has led to absorption mapping at lithospheric scale [2] and are considered important for the evaluation of the effective sensitivity in ambient noise imaging [12].

The space-weighting functions (SWF) discussed in this note are designed to be applied in the practice of the back-projection (or regionalization) method to retrieve the attenuation parameters in space [eg 9,13]. In this case, Q_i^{-1} and Q_s^{-1} estimated for a single source-receiver couple characterise the whole space volume, weighted by SWF values between 0 and 1. The SWF are designed with a Monte Carlo simulation of the multiple scattering process, following the method of Yoshimoto [14]. Each SWF value associated with a point in space for a single-station observation is proportional to the probability that at this point, the attenuation value is equal to the single-station observation. At a point in space, we thus have as many probabilities as observations. The average of all the observed values weighted by these SWF provides the value of attenuation at the point. These SWFs have been expressively designed to map scattering attenuation and absorption in volcanoes using a diffusion model and active sources [eg 4,15,16]. In the resulting models, the high-attenuation contrasts are often related to magma/fluid storage under volcanoes and ongoing volcano dynamics.

For a full discussion of the practice of attenuation mapping by weighted back-projection in volcanoes, the reader can refer to Del Pezzo *et al.* [17]. These authors obtain SWF for Q_i^{-1} and Q_s^{-1}. The two parameters can be rewritten using associated parameters, either the Seismic Albedo (B_0) and the Inverse-Extinction Length (Le^{-1}) or the intrinsic-(η_i) and scattering-(η_s) attenuation coefficients :

$$B_0 = \frac{\eta_s}{\eta_s + \eta_i} = \frac{Q_s^{-1}}{Q_i^{-1} + Q_s^{-1}}; Le^{-1} = \eta_s + \eta_i = \frac{2\pi f}{v}(Q_s^{-1} + Q_i^{-1}) \tag{1}$$

With a SWF, the spatial Q_i^{-1} and Q_s^{-1} are obtained using the following equations:

$$Q_s^{-1}[x,y] = \frac{\sum_k K_s^{2D}[x,y]_k Q_{sk}^{-1}}{\sum_k K_s^{2D}[x,y]_k} \tag{2}$$

$$Q_i^{-1}[x,y] = \frac{\sum_k K_i^{2D}[x,y]_k Q_{ik}^{-1}}{\sum_k K_i^{2D}[x,y]_k} \tag{3}$$

[1] Throughout this paper the syntactic rules used in Wolfram-Mathematica software for the use of parentheses is used: square brackets indicate the argument of a function; curly brackets indicate the elements of a matrix; round brackets indicate an algebraic grouping.

where K_i^{2D} and K_s^{2D} are the intrinsic and scattering SWF, Q_{ik}^{-1} and Q_{sk}^{-1} represent the estimates calculated from the fit of experimental Energy Envelopes with the diffusion model, and k spans the energy envelopes available. The uncertainties on the estimates of Q_{ik}^{-1} and Q_{sk}^{-1} can be propagated in equations (2) and (3) to estimate variances of $Q_i^{-1}[x,y]$ and $Q_s^{-1}[x,y]$, in the assumption of small covariance and null uncertainty in the determination of the weighting functions.

Del Pezzo *et al.* [17] additionally obtain that, in the case of a uniform half space and for diffusive propagation, the following function well approximates the numerically-calculated SWF for both absorption and scattering attenuation:

$$K_{i,s}^{2D}[x,y,x_r,y_r,x_s,y_s] = \frac{1}{4\pi\delta_x D^2\delta_y} exp\left[-\frac{\left(x-\frac{x_r+x_s}{2}\right)^2}{2\left(\delta_x D\right)^2} + \frac{\left(y-\frac{y_r+y_s}{2}\right)^2}{0.5\left(\delta_y D\right)^2}\right] + \frac{1}{2\pi\delta_x D^2\delta_y} exp\left[-\frac{(x-x_s)^2}{2\left(\delta_x D\right)^2} + \frac{(y-y_s)^2}{2\left(\delta_y D\right)^2}\right] + \frac{1}{2\pi\delta_x D^2\delta_y} exp\left[-\frac{(x-x_r)^2}{2\left(\delta_x D\right)^2} + \frac{(y-y_r)^2}{2\left(\delta_y D\right)^2}\right] \quad (4)$$

In equation (4), D is the source receiver distance, x and y are the space coordinates, x_s and y_s the source coordinate and x_r and y_r the receiver coordinates. The function fits reasonably well the numerically calculated SWF in case of short lapse time (around 15 s), highly diffusive media, and $\delta_x = \delta_y = 0.2$. These parameters represent the spatial aperture of the weighting function. The two numerically evaluated SWF have approximately the same shape once the level of heterogeneity increases (i.e., when the scattering processes approach the diffusion regime). This is contrary to what happens for lower heterogeneity [18,19] and is a result valid only for volcanoes and the active data geometry.

The spatial patterns described by the SWF depict the contribution of each cell to the coda formation and is thus proportional to the Sensitivity Kernels, respectively for scattering and intrinsic dissipation. Equation (4) is indeed equal that proposed at crustal scale for absorption mapping only at late lapse times [2,10,11]. The sensitivity is maximum at the source and receiver stations, remains high across the area contouring the seismic ray, then decreases at a distance controlled by the extinction length. This similarity in shape goes even further, as the spatial pattern of the function is identical to the depth-dependent diffusive sensitivity kernels in 3D defined by Obermann *et al.* [12]. The difference is in that the kernels do not assume a depth-dependent velocity structure, an approximation that is unfulfilled for shallow volcanic sources, but a constant velocity in a half-space approximation. The analytical solution of equation (4) is thus an approximate analytical equation for mapping Q_{coda}, similar in shape and meaning to those developed to map absorption. The equation was re-framed as a forward problem in a 5-km-deep volcanic medium [20] to map coda attenuation at Campi Flegrei caldera. The results of the inversion show the increased illumination provided by the technique and important correlations of the coda attenuation anomalies with deformation sources at the volcano.

The present note investigates how effective the SWF are to illuminate multi-scale volcanism in 3D. It is divided into three parts:

1. equation (4) is extended to the third dimension, maintaining the assumptions of shallow source and receiver in a diffusive Earth medium with no depth dependency - this is the case for the analysis of active seismic shots in volcanoes
2. we propose and discuss a SWF for mapping Q_{coda}, calculated for a deep source in a non-diffusive medium and discuss its limits;
3. we check the reliability and limits of the new approaches applying 3D SWFs to published seismic data bases. We use pre-calculated attenuation measurements for single source-station paths

from active data recorded at Deception Island volcano (Antarctica) [21] and volcano-tectonic earthquakes at Mount St. Helens volcano (USA) [22].

In Appendix, we report the main tests which were carried out in developing the applications. Test images are compared with previous tomography results obtained in the same areas using different seismic attributes, showing consistent features.

2. Results

2.1. 3D extension of the 2D weighting functions

2.1.1. Diffusive Earth media

We extended the numerical simulations described above to the third (depth) dimension, introducing the z-axis and keeping the half space approximation. For the assumption of no anomalous relevant depth dependency we rely on the results of [1]. The weighting function remains symmetrical around the axis connecting source to receiver, in analogy with the simulations using Radiative Transfer Theory [10] and alternative methods as SPECFEM3D [12]. This symmetry allows to evaluate the 3D SWF analytically for source (a shot) and receiver both placed at surface. In the case of a uniform half space, the function:

$$
\begin{aligned}
K^{3D}_{num}[x,y,z,x_r,y_r,x_s,y_s] = {} & \frac{1}{4\pi\delta_x D^3 \delta_y} \\
& exp\left[-\left(0.5\frac{\left(x-\frac{x_r+x_s}{2}\right)^2}{(\delta_x D)^2}+\frac{\left(y-\frac{y_r+y_s}{2}\right)^2}{(\delta_y D)^2}+\frac{(z^2)}{(\delta_z D)^2}\right)\right]+ \\
& \frac{1}{2\pi\delta_x D^3\delta_y\delta_z}Exp\left[-0.5\frac{(x-x_s)^2}{(\delta_x D)^2}+\frac{(y-y_s)^2}{(\delta_y D)^2}+\frac{z^2}{(\delta_z D)^2}\right]+ \\
& \frac{1}{2\pi\delta_x D^3\delta_y\delta_z}Exp\left[-0.5\frac{(x-x_r)^2}{(\delta_x D)^2}+\frac{(y-y_r)^2}{(\delta_y D)^2}+\frac{z^2}{(\delta_z D)^2}\right]
\end{aligned}
\tag{5}
$$

approximates the numerically calculated SWF in 3D to the first order (Figure 1). This analytical approximation is valid for the same range of Q_i and Q_s values and lapse time (15 s) used in Del Pezzo *et al.* [17]. This approximated space weighting function is actually a "kernel" function. Differently from the other diffusive kernels, it is valid solely for diffusive fields, short seismograms, and surface sources, like those recorded from shots fired in volcanoes for tomography purposes [21].

2.1.2. Deep sources (natural events) and non-diffusive fields

In the case of deep earthquakes, the assumptions made in calculating the approximation of SWF given by eq. (4) are invalid, and a multiple scattering regime better models coda-wave propagation. We thus adopt the Paasschens [23] approximation of the Energy Transport Equation solution in three dimensions to describe the seismogram Energy Envelope:

$$
\begin{aligned}
E^{3D}[r,t] \approx {} & \frac{W_0 exp[-Le^{-1}vt]}{4\pi r^2 v}\delta[t-\frac{r_{ij}}{v}]+W_0 H[t-\frac{r_{ij}}{v}]\cdot \\
& \frac{(1-\frac{r_{ij}^2}{v^2t^2})^{1/8}}{(\frac{4\pi vt}{3B_0Le^{-1}})^{3/2}}\cdot exp[-Le^{-1}vt]F[vtB_0Le^{-1}(1-\frac{r_{ij}^2}{v^2t^2})^{3/4}]
\end{aligned}
\tag{6}
$$

where

$$F[x] = e^x\sqrt{1+2.026/x}$$

and δ and H are the Dirac delta and the Heaviside step functions, respectively. Here, W_0 is the source energy and v is the seismic velocity. Fitting eq. (6) to the experimental energy envelopes, the single-path separate estimate of B_0 and Le^{-1} is possible in principle; however, in 2D, a severe trade-off affects the two parameters as discussed in Del Pezzo *et al.* [17]. An alternative is the use of a simplified formula, which estimates Le^{-1} and B_0 from the fit of data to the first order approximation of the Energy Transport model equation, as given by Zeng *et al.* [24]:

$$E[r,t,B0,Le^{-1},v] = \frac{\delta[r-vt]}{4\pi v r^2}Exp[-rLe^{-1}]+ H[r/v]\frac{B_0Le^{-1}}{4\pi rvt}Log[\frac{1+r/vt}{1-r/vt}]Exp[-vtLe^{-1}]. \tag{7}$$

With such a fit, the severe trade-offs disappear. Equation (7) is equivalent to the single-scattering model developed by Sato [25] and is valid for low heterogeneity and short lapse times. In this case, intrinsic attenuation controls Le^{-1}, being η_s small. The physical meaning of the retrieved B_0 and Le^{-1} becomes controversial when energy envelopes recorded in media with high heterogeneity are modelled with equation (7). In this case, the fit-function is based on improper assumptions and Le^{-1} is proportional to the widely measured Q_{coda}, the coda quality factor [25] used to map, e.g., different tectonic settings at crustal scale [1].

The downside is that Q_{coda} is not a physical parameter of the propagation medium; however, the Le^{-1} (or Q_{coda}) space distribution can still depict attenuation properties, and the corresponding SWF, K_{coda}, can be calculated. For this task, we use the hypothesis of Pacheco and Snieder [26], setting B_0 at an average value and $Le^{-1} \cong \frac{2\pi f}{v}Q^{-1}_{coda}$:

$$K^{3D}_{coda,k}[\varrho,T,B_0,Le^{-1},v] = \int_0^T E[r_{s\varrho},\tau,B_0,Le^{-1},v]E[r_{\varrho r},T-\tau,B_0,Le^{-1},v]d\tau \tag{8}$$

where ϱ is the space point with coordinates $\{x,y,z\}$, T is the lapse time, τ is the integration variable (time). The integral can be numerically calculated. In Figure A1, we show the contour plot of Q_{coda} as a function of Q_i^{-1} and Q_s^{-1}. For low scattering attenuation, Q^{-1}_{coda} is independent of Q_s^{-1} and similar to Q_i^{-1} (see Appendix, Figure A1, left panel). An increase of scattering (right panel) increases the trade-off. In Figure 2, we reproduce the SWF calculated using equation (8).

2.2. Application examples

The final Q_{coda} image as a function of the space coordinates in a 3D space is thus obtained with a back-projection analogue to that used in equations 2 and 3:

$$Q^{-1}_{coda}[x,y,z] = \frac{\sum_k K^{3D}_{coda,k}[x,y,z]Q^{-1}_{coda,k}}{\sum_k K^{3D}_{coda,k}[x,y,z]} \tag{9}$$

where K^k_{coda} is the weighting function for the k-th source-receiver couple and $Q^{-1}_{coda,k}$ is the k-th Q_{coda} estimate. k spans over the available source-receiver couples. To avoid confusion with respect to the definition of source-station kernels we remind the reader that:

1. the values of $K^{3D}_{coda,k}[x,y,z]$ express the *probability* that the Q^{-1}_{coda} estimated at a station is equal to the one measured at [x,y,z];
2. equation (9) is to be used exclusively for back-projection;
3. the kernel $K^{3D}_{num}[x,y,z,x_r,y_r,x_s,y_s]$ in equation (5) can still be used in an inversion for the space-dependent parameters, if the underlying hypotheses are fulfilled.

2.2.1. Deception Island volcano - diffusive approximation

Deception Island volcano (Antarctica) is an extraordinary natural laboratory, characterised by a horseshoe shape which permits to design seismic active field surveys characterized by elaborate source and receiver geometries. To test the 3D SWF discussed in this note, we used data from the seismic experiment TOMO-DEC [21] publicly available from the Australian Antarctic Data Center repository (AADC). The same data set was used by Prudencio *et al.* [16], who obtained a first 2D attenuation image of this island using a simplified (Gaussian shape) SWF (data and final models also are available from the AADC repository). Del Pezzo *et al.* [17] improved this image using the 2D weighting function of equation (4), applied to data filtered in several frequency bands centred from 4 to 20 Hz. The present test is carried out using data filtered in the 4 Hz band, where the highest attenuation contrasts were previously observed. Using the 3D SWF of equation (5), we show the attenuation coefficient space distribution calculated at depths of 2 and 4 km, with a horizontal grid of 4 km (Figure 3). The two panels are similar, with high absorption affecting the Eastern and Southwestern parts of the Island. Because the SWF are practically null at 6 km, no images can be calculated below this depth.

2.2.2. 3D SWF at Mount St. Helens volcano - non-diffusive media

Mount St. Helens volcano (US) is a central-cone stratovolcano, characterized by 0-7 km deep earthquakes (under the central cone) and lateral fault seismicity (down to 20 km). A 3D Q_c^{-1} attenuation model of the area has been calculated using the SWF described by equation (8) through equation (9) at Mount St. Helens, with a test passive dataset of 451 waveforms ([27] - available from the PANGAEA Data Centre). We use the single-path Q_{coda} estimates obtained by De Siena *et al.* [3] at 6 Hz. In Appendix, the sensitivity test carried out to check the reliability of the method is described. Equation (9) has been applied to a space grid with space points separated by a distance of 4 km. In this way, we obtain the Q_{coda} space values at 500 3D grid points. The Q_{coda}^{-1} 3D space distribution is plotted on two horizontal slices, crossing the z axis at depths of 0.5 km and 4 km (Figure 4, uppermost panels). The vertical slice (lower panel) intersects the surface along the white line drawn in the upper left panel. A sensitivity test using a hemispherical anomaly centred in the middle of the study area is described in Appendix. The input test is only roughly reproduced: the small number of data available would correspond to an underdetermined inversion problem, and this strongly reduces the sensitivity of the method to small anomalies, making unsuccessful any checkerboard test.

3. Discussion

Figure 1 shows that, in areas of high heterogeneity (diffusion approximation) and for data shots fired at the surface, the sensitivity of the SWF method strongly reduces for increasing depth, as the SWF values strongly decrease with depth. Coda waves recorded from shots fired at the surface in diffusive Earth media and recorded at short distances, as for the Deception Island case study, propagate mainly in the upper 3 - 4 kilometres of the crust (Figure 3). The Northern part of the island is associated with the crystalline basement and shows low attenuation, while high-attenuation bodies, spatially-correlated to high-velocity structures (Ben-Zvi *et al.* 28;Zandomeneghi *et al.* 29) characterise the southern part of the volcano. There is a consistent agreement between low/high coda attenuation and high/ low-velocity structure since the first scattering/absorption separations [16]. The correlation between the SWF-dependent 2D models [17] and the 3D models indicates that coda-attenuation estimates are stable using this dataset. Comparing the present 3D attenuation images with the total-Q images obtained by Prudencio *et al.* [30] using direct-P coda-normalized waves (MuRAT code - De Siena *et al.* [31]) we observe a good match between the 3D intrinsic-Q and the total-Q distributions. The location of the main total high-attenuation body retrieved by Prudencio *et al.* [30] spatially fits the main absorption anomaly.

To investigate greater depths, deeper sources (passive data) are necessary. In this case, the diffusion equation is inappropriate, as the Earth heterogeneity strongly reduces with depth and a theory based on multiple scattering is necessary. However, inverting a multiple scattering model for energy envelopes associated with single source-receiver couples prevents the recovery of separate scattering and intrinsic tomography images due to the trade-off between $B0$ and Le^{-1}. The only possibility is thus the use of an approximate kernel to invert for a unique parameter, Le^{-1}, a quantity proportional to the widely measured Q_{coda} parameter. In this case, we proposed to calculate the corresponding SWF using the approach described by Pacheco and Snieder [26]: despite the controversial physical meaning of Q_{coda}, images of the spatial variations of Q_{coda} are still retrievable, like those recently described by Mayor *et al.* [2] which depict the attenuation structure of the Alps. Following this approach, we calculated the 3D Q_{coda} image of Mount St. Helens volcano (Figure 4). We compared them on a map with the 2D Q_{coda} space distribution obtained by De Siena *et al.* [3]. The authors used maps of late lapse-time Q_{coda}, assuming it as a measurement of absorption, and energy-envelope peak-delays, a quantity proportional to scattering-Q, to separate scattering attenuation from absorption. They back-project the single-station Q_{coda} values assuming that it is distributed on a strip connecting source and ray, derived from pre-calculated 3D rays.

At both depths shown in Figure 4, the low inverse Q_{coda} west of Mount St. Helens is a major feature, similar to that observed by De Siena *et al.* [3] (see their Figure 5, 6 Hz panel). Nevertheless, this area is a unique anomaly in our analysis, located west of the volcano at a depth of 4 km, and extends to the south at 500 m. A wide area inside this anomaly was not sampled in the previous study, as it assumed a back-projection of the single-station Q_{coda} along a strip. In the case of Mount St. Helens, many of the seismic sources are located at, or below, 8 km; the SWF theoretically produce an improved resolution in this depth range due to the wider illumination at near-source nodes. The example reported in the present paper is made with a limited number of data. The images obtained for Mount St. Helens are thus defocused and need to be improved using a greater data set. Despite this limitation, the use of SWF's is promising in enlightening the space attenuation contrasts. We are confident that it may become a useful tool to complement tomography images achieved with different techniques, especially due to its independence of velocity tomography results.

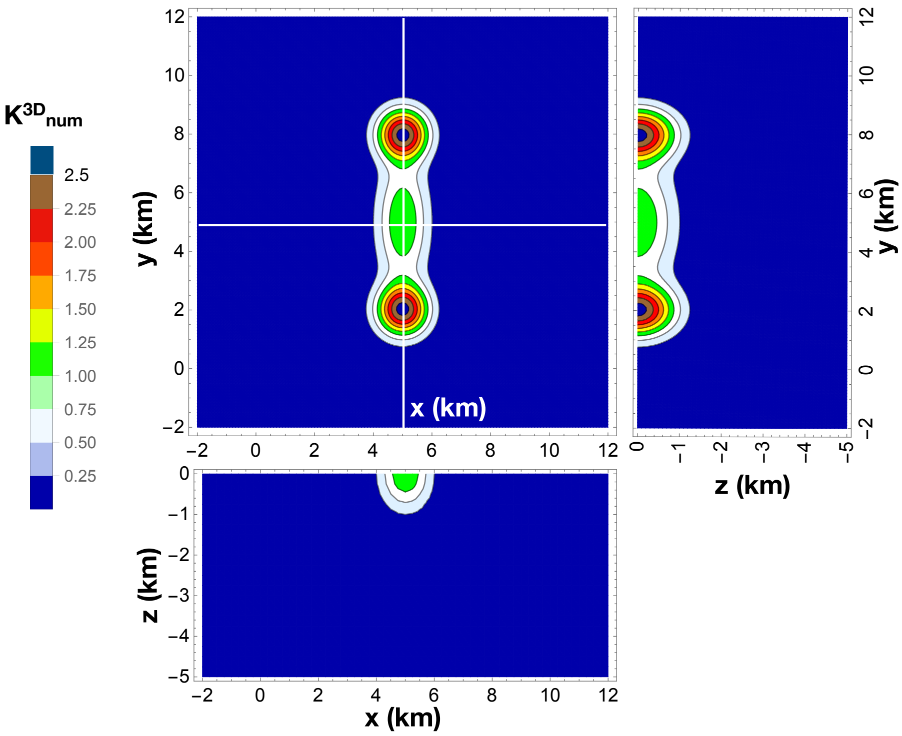

Figure 1. Plot of the 3D kernel function obtained using Equation 5. The source and receiver are set at [xs=5km, ys=2km] and [xr=5 km,yr=8 km], respectively. The colour-scale marks the isosurfaces. The kernel function is normalized to its value at [x=5 km, y=5 km]. The vertical sections correspond to the white lines shown on the x-y plane.

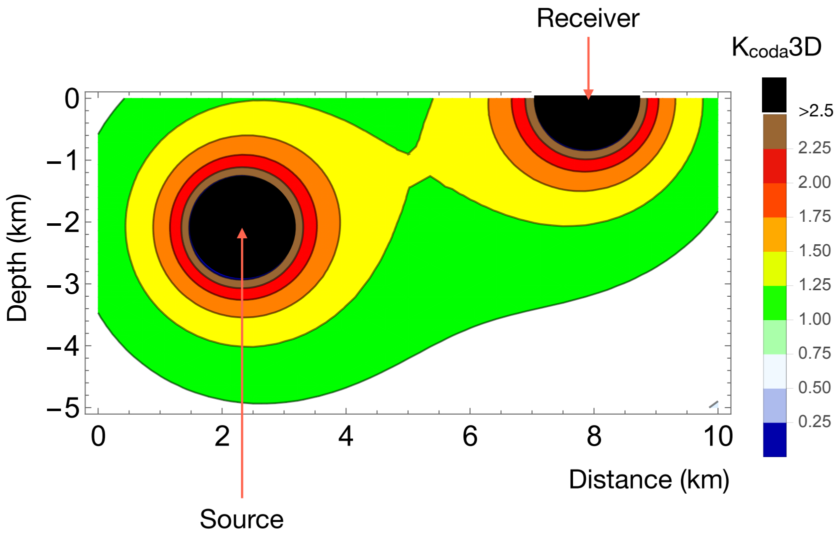

Figure 2. Vertical section showing the 3D kernel function obtained using Equation 8. The colour-scale marks the isosurfaces. The kernel function is normalized to its value at [x=5 km, z=-2.5 km].

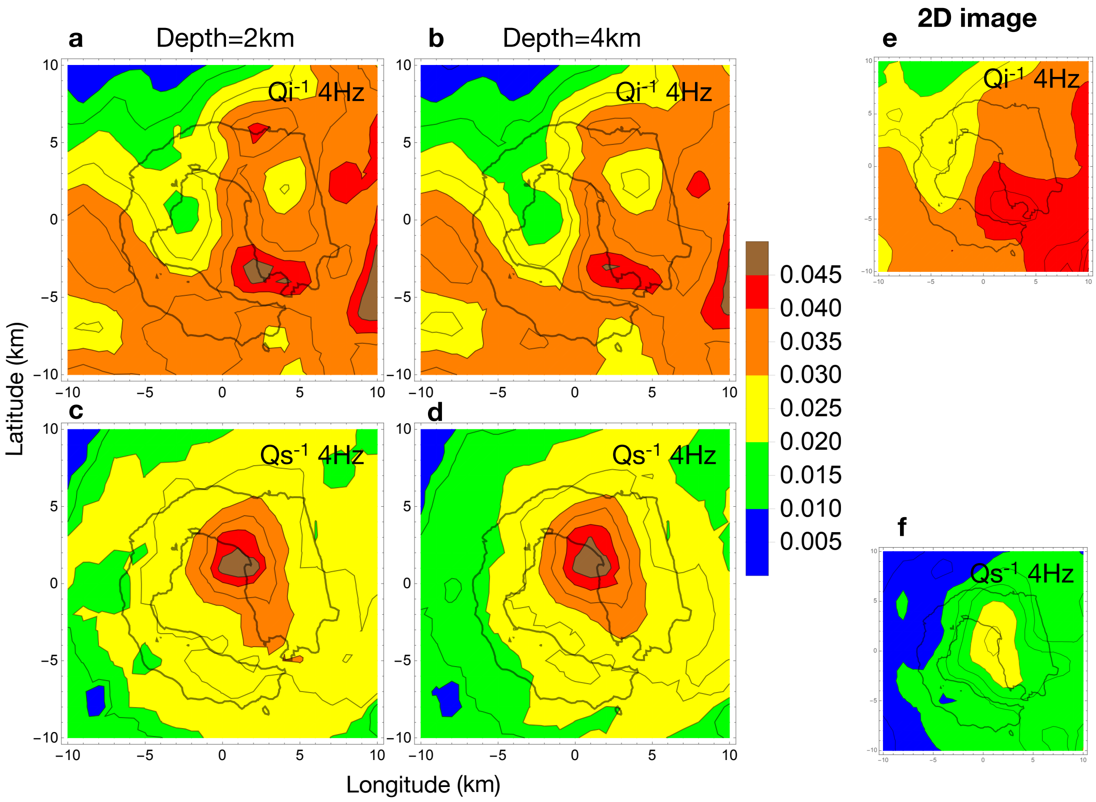

Figure 3. The three-dimensional images obtained for Deception Island at 4 Hz are compared with the bi-dimensional images in Del Pezzo et al., 2016. Horizontal slices cut the Q_i^{-1} (a,b) and Q_s^{-1} (c,d) models at depths of 2 km and 4km, respectively. The 2D Q_i^{-1} (e) and Q_s^{-1} (f) models from Del Pezzo *et al.* [17] are redrawn for comparison using the same colour scale. We use the same distribution of sources and receivers shown in Prudencio *et al.* [15].

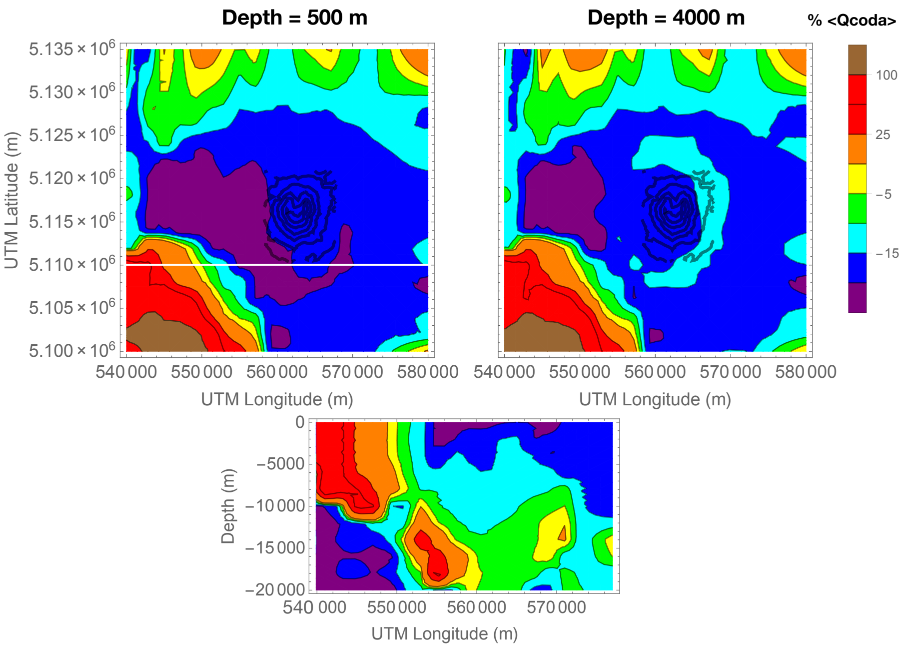

Figure 4. Q_{coda}^{-1} space distribution at Mount St. Helens. Horizontal slices calculated at the depths of 0.5 km and 4.0 km. The vertical section intersects the horizontal plane along the white line in the upper left panel. Topography isolines (only in the zone of Mount St. Helens) are superimposed. Discrete Q_{coda}^{-1} space distribution has been interpolated before plotting the percent of average inverse Q_{coda}, $< Q_{coda}^{-1} >$. All panels are drawn using Mathematica_10^{TM}.

4. Materials and Methods

Acknowledgments: This research was partly supported by the Projects TEC2015-68752 (MINECO/FEDER), TEC2015-68752 (KNOWAVES).

Author Contributions: Edoardo Del Pezzo wrote the paper together with Francesca Bianco, Jesus Ibanez and Luca De Siena. Edoardo del Pezzo, Simona Gabrielli and Luca De Siena analyzed the data and calculated the 3D SWF-derived models for all the examples reported. Angel de La Torre wrote the software reported in the supplementary Material implementing the SWF

Conflicts of Interest: The authors declare no conflict of interest.

Abbreviations

The following abbreviations are used in this manuscript:

SWF Space-Weighthed Functions

Appendix A Demonstration that Q_{coda}^{-1} approaches Q_i^{-1} in media with small Q_s^{-1}

We have fit the Paasschens model calculated for several couples $\{Q_i^{-1}, Q_s^{-1}\}$ to the Aki and Chouet's formula [32] and inverted for Q_{coda}. The Q_{coda} contours are shown in Figure A.1. Vertical contours in the left panel show that, independently of Q_s^{-1}, Q_i practically coincides with Q_{coda}.

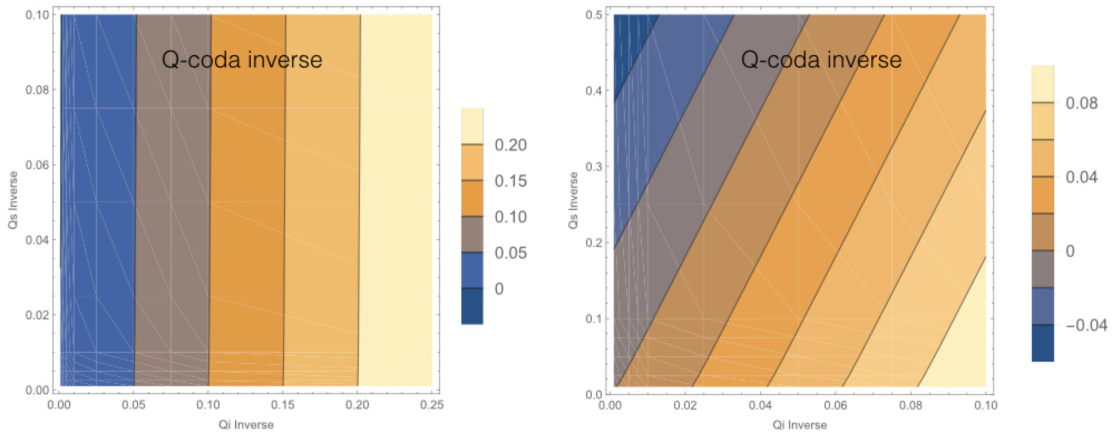

Figure A.1. Left. Q_{coda}^{-1} in media with low values of Q_s^{-1} is independent of Q_s^{-1}. Right. In case of high scattering attenuation (approaching to the diffusion regime) the plots show some trade-off.

Appendix B Sensitivity tests for 3D Q_{coda} SWF

At Deception Island, we use as input checkerboard structure laterally-extended 4x4 km, parallelepipeds, extending down to 10 km depth (Figures B.1). Q-values alternate between 50 and 500. We do not report the results obtained for inputs with a cell structure alternate in depth, as the SWF for shallow source and receiver are about zero below 6 km, producing false uniform structures at increasing depth. At Mount St. Helens, the available data set is much smaller than at Deception Island. The corresponding sensitivity tests thus show that the SWF calculated using with Equation 8 do not reproduce the input values adequately, mainly because the poor sampling in space affects the averaging process described by Equation 2. Despite this limitation, the input values are reproduced in the central part of the area (i.e. the volcanic edifice). The input values are underestimated elsewhere, with blurring and ghosts emerging around the volcano.

At Mount St. Helens (Figure B.2) we built as second synthetic input a hemisphere with a contrast in Q of $\frac{1}{5}$ with respect to the background. The process of averaging yields a blurred image on the sides; the vertical profile shows a similar contrast with respect to input down to 10 km, with consistent ghosts to the side and deeper than the central anomaly. A greater number of data would improve the image definition, as the SWF map the structures around the central cone insufficiently.

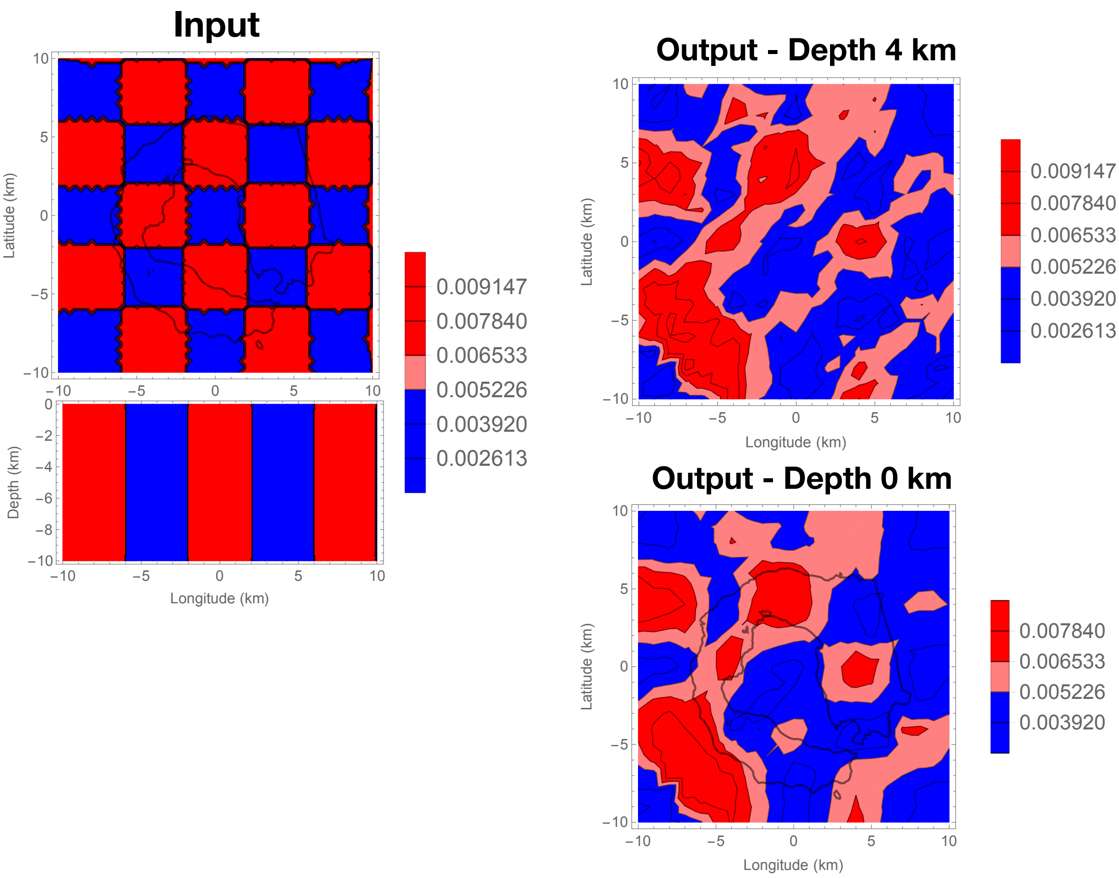

Figure B.1. Synthetic test for the SWF. Left panels: input. Right panels: output.

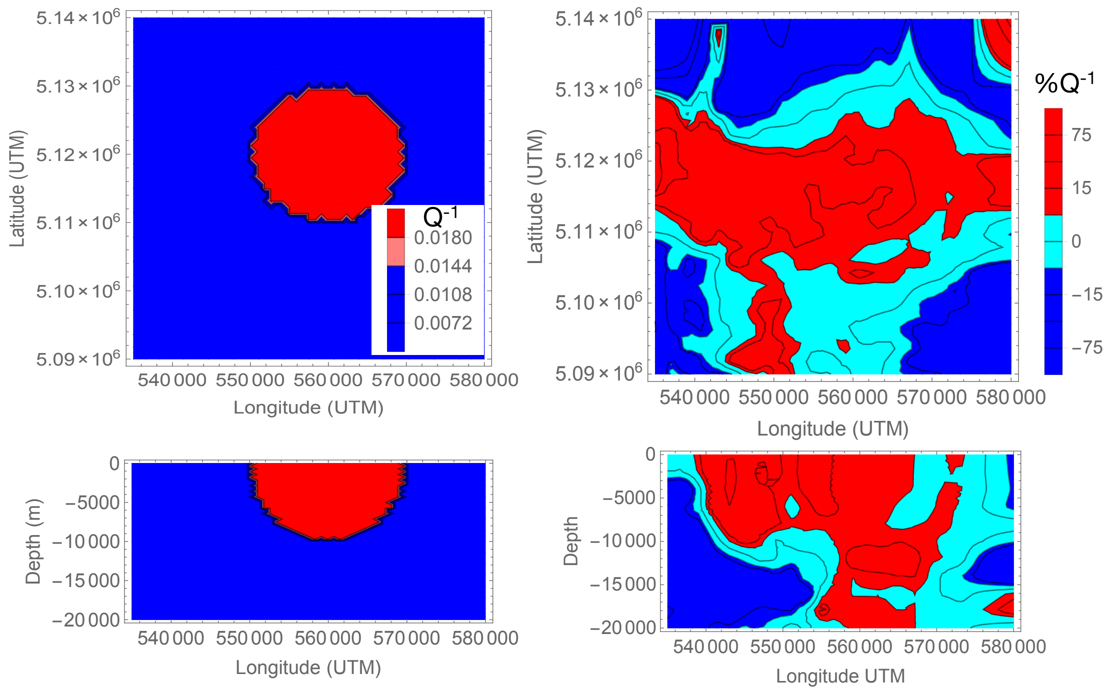

Figure B.2. Synthetic test. Left panels: test input, where the contrasts are expressed as percent respect to the average. and correspond to $Q = 50$ (red) and $Q = 500$ (blue). Right panels: output, where the attenuation contrast is reproduced only in the center of the area.

Appendix C Numerical integration of equation (8)

The function to be integrated (equation 8) is a product of two functions, each one including a delta and a continuously decaying term, which here we call "coda". Hereafter we drop out in equation (8) the dependence on B_0, Le^{-1} and v leaving unaltered ϱ and t. Therefore, the integral $K_{ss}[\varrho, t]$ can be decomposed into four integrals (i.e. delta·delta, delta·coda, coda.delta and coda.coda):

$$K_{ss}[\varrho, t] = I_1[\varrho, t] + I_2[\varrho, t] + I_3[\varrho, t] + I_4[\varrho, t] \tag{A1}$$

each of them null for $t < (t_a + t_b)$ where t_a and t_b are respectively the time the perturbation reaches position ϱ from the source and the time from ϱ to receiver. These integrals are defined as:

$$\begin{aligned}
I_1[\varrho, t] &= \int_{t_a+t_b}^{t} E_1[r_a, u]\delta[u - t_a]E_1[r_b, t - u]\delta[t - u - t_b]du \\
I_2[\varrho, t] &= \int_{t_a+t_b}^{t} E_1[r_a, u]\delta[u - t_a]E_2[r_b, t - u]du \\
I_3[\varrho, t] &= \int_{t_a+t_b}^{t} E_2[r_a, u]E_1[r_b, t - u]\delta[t - u - t_b]du \\
I_4[\varrho, t] &= \int_{t_a+t_b}^{t} E_2[r_a, u]E_2[r_b, t - u]du
\end{aligned}$$

where $E_1[r, t]$ refers to the wavefront (or delta) contribution, $E_2[r, t]$ refers to the coda contribution, $[r_a, t_a]$ refers to the source-ϱ impulsive response and $[r_b, t_b]$ refers to the ϱ-receiver impulsive response.

Taking into account the sampling property of the Dirac's delta function:

$$\int \delta[u - t_0]f[u]du = f[t_0]$$

the integrals $I_1[\varrho, t]$, $I_2[\varrho, t]$ and $I_3[\varrho, t]$ can easily be solved:

$$I_1[\varrho, t] = E_1[r_a, t_a]E_1[r_b, t_b]\delta[t - t_a - t_b] \tag{A2}$$

$$I_2[\rho, t] = E_1[r_a, t_a]E_2[r_b, t - t_a] \tag{A3}$$

$$I_3[\varrho, t] = E_1[r_b, t_b]E_2[r_a, t - t_b] \tag{A4}$$

It can be demonstrated that if functions $E^{3D}[r_a, t]$, $E^{3D}[r_b, t]$ are known, then $I_1[\varrho, t]$, $I_2[\varrho, t]$ and $I_3[\varrho, t]$ are immediately known and easily evaluable functions.

The last integral $I_4[\varrho, t]$ is obtained by convolving both codas. It is a continuous function with null value for $t < (t_a + t_b)$ and with an exponential decay for large times. Its computation requires a numerical integration to solve the convolution. The entire procedure with all the demonstrations is reported in (De La Torre and del Pezzo, in preparation. A pre-print draft can be requested to the authors). The Matlab code to perform the calculation is reported in the supplementary material, together with the entire algorithm estimating the SWF as a function of the 3D space coordinates, with Le^{-1},B_0 and v as parameters.

1. Calvet, M.; Sylvander, M.; Margerin, L.; Villasenor, A. Spatial variations of seismic attenuation and heterogeneity in the Pyrenees: Coda Q and peak delay time analysis. *Tectonophysics* **2013**, *608*, 428–439.
2. Mayor, J.; Calvet, M.; Margerin, L.; Vanderhaeghe, O.; Traversa, P. Crustal structure of the Alps as seen by attenuation tomography. *Earth and Planetary Science Letters* **2016**, *439*, 71 – 80.
3. De Siena, L.; Calvet, M.; Watson, K.J.; Jonkers, A.R.T.; Thomas, C. Seismic scattering and absorption mapping of debris flows, feeding paths, and tectonic units at Mount St. Helens volcano. *Earth And Planetary Science Letters* **2016**, *442*, 21–31.
4. Prudencio, J.; Del Pezzo, E.; Ibanez, J.; Giampiccolo, E.; Patane, D. Two-dimensional seismic attenuation images of Stromboli Island using active data. *Geophysical Research Letters* **2015-a**, *42*.
5. Del Pezzo, E.; Ibáñez, J.; Morales, J.; Akinci, A.; Maresca, R. Measurements of intrinsic and scattering seismic attenuation in the crust. *Bulletin Of The Seismological Society Of America* **1995**, *85*, 1373–1380.
6. Akinci, A.; Del Pezzo, E.; Ibañez, J. Separation of Scattering and Intrinsic Attenuation in the Southern Spain and Western Anatolia (Turkey). *Geophysical Journal International* **1995**, *121*, 337–353.
7. Wegler, U.; Luhr, B. Scattering behaviour at Merapi volcano(Java) revealed from an active seismic experiment. *Geophysical Journal International* **2001**.
8. Lacombe, C.; Campillo, M.; Paul, A.; Margerin, L. Separation of intrinsic absorption and scattering attenuation from Lg coda decay in central France using acoustic radiative transfer theory. *Geophysical Journal International* **2003**, *154*, 417–425.
9. Xie, J.; Mitchell, B. A Back-Projection Method for Imaging Large-Scale Lateral Variations of Lg Coda Q with Application to Continental Africa. *Geophysical Journal International* **1990**, *100*, 161–181.
10. Margerin, L.; Planes, T.; Mayor, J.; Calvet, M. Sensitivity kernels for coda-wave interferometry and scattering tomography: theory and numerical evaluation in two-dimensional anisotropically scattering media. *Geophys. J. Int.* **2016**, *204*, 650–666.
11. Rossetto, V.; Margerin, L.; Planès, T.; Larose, É. Locating a weak change using diffuse waves (LOCADIFF): theoretical approach and inversion procedure. *Arxiv preprint arXiv:1007.3103* **2010**.
12. Obermann, A.; Planès, T.; Larose, E.; Sens-Schönfelder, C.; Campillo, M. Depth sensitivity of seismic coda waves to velocity perturbations in an elastic heterogeneous medium. *Geophysical Journal International* **2013**, *194*, 372–382.
13. Singh, S.; Herrmann, R.B. Regionalization of Crustal Coda Q in the continental United States. *Journal of Geophysical Research* **1983**, *88*, 527–538.
14. Yoshimoto, K. Monte Carlo simulation of seismogram envelopes in scattering media. *JOURNAL OF GEOPHYSICAL RESEARCH* **2000**.
15. Prudencio, J.; Del Pezzo, E.; Garcia Yeguas, A.; Ibanez, J.M. Spatial distribution of intrinsic and scattering seismic attenuation in active volcanic islands - I: model and the case of Tenerife Island. *Geophysical Journal International* **2013-a**, *195*, 1942–1956.
16. Prudencio, J.; Ibanez, J.M.; Garcia Yeguas, A.; Del Pezzo, E.; Posadas, A.M. Spatial distribution of intrinsic and scattering seismic attenuation in active volcanic islands - II: Deception Island images. *Geophysical Journal International* **2013-b**.
17. Del Pezzo, E.; Ibañez, J.; Prudencio, J.; Bianco, F.; De Siena, L. Absorption and scattering 2-D volcano images from numerically calculated space-weighting functions. *Geophys. J. Int* **2016**, *206*, 742–756.
18. Sato, H. Study of seismogram envelopes based on scattering by random inhomogeneities in the lithosphere: a review. *Physics Of The Earth And Planetary Interiors* **1991**.
19. Hoshiba, M. Simulation Of Multiple-scattered Coda Wave Excitation Based On The Energy-conservation Law. *Physics Of The Earth And Planetary Interiors* **1991**, *67*, 123–136.
20. De Siena, L.; Amoruso, A.; Pezzo, E.D.; Wakeford, Z.; Castellano, M.; Crescentini, L. Space-weighted seismic attenuation mapping of the aseismic source of Campi Flegrei 1983–1984 unrest. *Geophysical Research Letters* **2017**, *44*, 1740–1748.
21. Ibañez, J.M.; Díaz-Moreno, A.; Prudencio, J.; Zandomeneghi, D.; Wilcock, W.; Barclay, A.; Almendros, J.; Benítez, C.; García-Yeguas, A.; Alguacil, G. Database of multi-parametric geophysical data from the TOMO-DEC experiment on Deception Island, Antarctica. *Scientific Data* **2017**, *4*, 170128–18.

22. De Siena, L.; Thomas, C.; Aster, R. Multi-scale reasonable attenuation tomography analysis (MuRAT): An imaging algorithm designed for volcanic regions. *Journal Of Volcanology And Geothermal Research* **2014-b**, *277*, 22–35.
23. Paasschens, J. Solution of the time-dependent Boltzmann equation. *Physical Review E* **1997**, *56*, 1135–1141.
24. Zeng, Y.; Su, F.; Aki, K. Scattering wave energy propagation in a random isotropic scattering medium. Part 1. Theory. *Journal Of Geophysical Research-Solid Earth* **1991**, *96*, 607–619.
25. Sato, H. Single isotropic scattering model including wave convesions Simple theoretical model of the short period body wave propagation. *J.Phys.Earth* **1977**, *25*, 163–176.
26. Pacheco, C.; Snieder, R. Time-lapse travel time change of multiply scattered acoustic waves. *J. Acoust. Soc. Am.* **2005**, *118*, 1300 – 1310.
27. De Siena, L.; Thomas, C.; Waite, G.P.; Moran, S.C.; Klemme, S. Attenuation and scattering tomography of the deep plumbing system of Mount St. Helens. *Journal Of Geophysical Research-Solid Earth* **2014-b**, *119*, 8223–8238.
28. Ben-Zvi, T.; Wilcock, W.S.D.; Barclay, A.H.; Zandomeneghi, D.; Ibanez, J.M.; Almendros, J. The P-wave velocity structure of Deception Island, Antarctica, from two-dimensional seismic tomography. *Journal Of Volcanology And Geothermal Research* **2009**, *180*, 67–80.
29. Zandomeneghi, D.; Barclay, A.; Almendros, J.; Godoy, J.M.I.; Wilcock, W.S.D.; Ben-Zvi, T. The Crustal Structure of Deception Island Volcano from P-wave Seismic Tomography: Tectonic and Volcanic Implications. *Journal of Geophysical Research-Solid Earth* **2009**, *114*, 16.
30. Prudencio, J.; De Siena, L.; Ibanez, J.M.; Del Pezzo, E.; Garcia Yeguas, A.; Díaz-Moreno, A. The 3D Attenuation Structure of Deception Island (Antarctica). *Surveys in Geophysics* **2015-b**, *36*, 371–390.
31. De Siena, L.; Thomas, C.; Aster, R. Multi-scale reasonable attenuation tomography analysis (MuRAT): An imaging algorithm designed for volcanic regions. *Journal Of Volcanology And Geothermal Research* **2014-a**, *277*, 22–35.
32. Aki, K.; Chouet, B. Origin of coda waves: Source, attenuation, and scattering effects. *Journal Of Geophysical Research-Solid Earth* **1975**, *80*, 3322–3342.